Experimental demonstration of highly localized pulses (X waves) at microwave frequencies

Nikolaos Chiotellis, Victor Mendez, Scott M. Rudolph, and Anthony Grbic

Phys. Rev. B **97**, 085136 — Published 20 February 2018

DOI: 10.1103/PhysRevB.97.085136

Experimental Demonstration of X Waves at Microwave Frequencies

Nikolaos Chiotellis[1], Victor Mendez[2], Scott M. Rudolph[2], and Anthony Grbic[1*]
[1] *Department of Electrical Engineering and Computer Science, University of Michigan, Ann Arbor, Michigan, USA*
[2] *US Naval Research Laboratory, Washington, DC, USA*

(Dated: January 26, 2018)

A device that radiates transverse magnetic Bessel beams in the radiative near field is reported. The cone angle of the emitted radiation remains constant over a wide frequency range (18-30 GHz), allowing highly localized pulses (X Waves) to be generated under a broadband excitation. The design process, based on ray optics, is discussed. Both frequency and time domain experimental results from a prototype are presented. The measured fields show close agreement with simulation results and demonstrate the radiator's ability to emit X Waves within its nondiffracting range.

Since the seminal work of Brittingham[1], numerous advancements have been made in the area of Localized Waves (LW)[2]. Such waves resist diffraction and, as a result, maintain their field profile as they propagate. Brittingham introduced Focus Wave Modes as packet-like solutions to Maxwell's equations that remain focused as they propagate. Ziolkowski addressed the issue of infinite energy possessed by these solutions by superimposing them to construct Electromagnetic Directed-Energy Pulse Trains of finite energy[3].

In his work on Electromagnetic Missiles, Wu manipulated the rise time of a radiating aperture to generate fields that decay slower than $1/r^4$. He did so by effectively extending the radiative near field (where such phenomena can occur) to larger distances. Electromagnetic Bullets, introduced by Moses and Prosser, are solutions to the wave equation that are confined to a cone[5]. These energy packets have the classical $1/r$ field decay, but remain localized along a ray path.

Durnin revolutionized the field of Localized Waves by introducing Bessel beams, which are superluminal, monochromatic solutions to the wave equation that do not diffract[6]. Although ideal Bessel beams cannot be generated, since they require infinite energy, their truncated counterparts are realizable and resist diffraction over a specified distance called the nondiffracting range. A Bessel beam propagating along an axis results from the interference of all the plane waves that form a specific angle, called the cone angle, with the axis. This angle determines the phase and group velocity of the wave, and, together with the size of the aperture, determine the nondiffracting range.

Since their discovery, Bessel beams have been used in many practical applications. Originally, researchers envisioned using them for medical ultrasonic imaging, tissue characterization and nondestructive evaluation of materials[7]. More recent applications include optical conveyors[8], electron microscopy[9], microfabrication of dielectrics[10], exerting forces on biological cells[11], and optical communications[12].

Bessel beams can be generated through a range of techniques. At microwave frequencies, axicons[13], leaky wave antennas[14], cascaded metasurfaces[15], and GRIN lenses[16] have been used among other techniques. At optical frequencies, researchers have employed axicons[17], plasmonic metasurfaces[18], localized modes[19], and holography[20].

A superposition of Bessel beams with a common cone angle over a range of frequencies yields localized pulses known as X Waves, first introduced by Lu and Greenleaf[21]. All frequency components of an X Wave travel at the same velocity. As a result, these pulses resist both diffraction (spatial spreading) and dispersion (temporal spreading), and remain confined as they propagate.

Although multiple techniques/structures have been suggested for the generation of Bessel beams, little progress has been made on the generation of X Waves outside of optical frequencies[22,23]. At microwave frequencies, a radial line slot antenna was proposed in[24], whose bandwidth is limited by the frequency dispersion of the radial waveguide. In general, the minimum cone angle that can be achieved with leaky wave structures is also limited by their high attenuation rate for radiation near broadside. A microwave system using a circular slit and a parabolic mirror was used in[25] to verify the superluminal behavior of X Waves.

In order to generate X Waves at microwave frequencies, a device must exhibit a large bandwidth and minimal dispersion within that bandwidth. Designing a directly fed radiator would be advantageous since it would occupy less space than an illuminated transmissive or reflective device. Finally, the device should operate efficiently.

Ultrawideband systems such as those used in radars, medical imaging, or digital communications, employ broadband antennas designed to operate in the far field[26]. In general, the radiating elements of these systems have low directivity. On the contrary, antennas operating in the radiative near field (Fresnel zone) have been developed for narrowband applications, e.g. radiometry[27], RFID[28] and focusing systems[29]. Here, a radiator with 50% fractional bandwidth is developed to generate spatially confined fields in the Fresnel zone. Unlike the earlier works[22,23,25], the radiated beam exhibits a well-defined transverse magnetic (TM) polarization and the modal purity of a single dominant Bessel beam mode. When fed with a broadband pulse, the radiator emits

non-dispersive, nondiffracting X Waves.

The proposed Bessel beam radiator generates φ-invariant Bessel beams. As a result, its design (depicted in Fig. 1(a)) is rotationally symmetric about the z-axis. The device is fed by a coaxial cable with inner and outer radii equal to r_{in} and r_{out}, respectively, as shown in the inset of Fig. 1(a). The green region corresponds to the insulator within the coaxial cable. The inner conductor of the coaxial cable is extended by a length p to form an electrically small monopole. The outer conductor of the coaxial cable is flared outwards, forming an angle φ_1 with respect to the z-axis. The blue region, into which the monopole radiates, is filled with a material of dielectric constant ε_r. At every point along the curved air-dielectric interface, the tangent line forms an angle φ_2 with respect to the z-axis. The height of the device is h. A cutaway three-dimensional view of the design is shown in Fig. 1(b). An earlier version of this device having a straight interface was presented in[30]. The radiator presented here exhibits higher spectral purity.

Consider a ray emanated by the radiating monopole at an angle θ_1 with respect to the z-axis. The ray is totally internally reflected by appropriately selecting the dielectric constant ε_r. It is then directed toward the copper cladding of the device and reflected back toward the interface. When it reaches the interface for a second time, the ray forms a much smaller angle with the air-dielectric interface, and exits at an angle θ_2 with respect to the z-axis. Assuming that a unique curvature angle φ_2 corresponds to each ray angle θ_1 (an assumption that can be shown to hold when the range of φ_2 is small), the cone angle, θ_2, can be written as:

$$\theta_2(\theta_1) = 90^\circ - \varphi_2(\theta_1) - \sin^{-1}\left(\sqrt{\varepsilon_r}\cos(3\varphi_2(\theta_1) - 2\varphi_1 - \theta_1)\right). \quad (1)$$

The dielectric constant of the material is chosen to be $\varepsilon_r = 2.53$, which corresponds to Rexolite®: a low loss polymer ($\tan\delta = 0.00066$ at 10 GHz). The cone half-angle is set to $\varphi_1 = 32.5^\circ$ for impedance matching purposes. Eq. 1 is then numerically solved for ray angles ranging from $\theta_1 = 0^\circ$ to $\theta_1 = \varphi_1 = 32.5^\circ$ to find the curved interface that yields a constant cone angle of $\theta_2 = 20^\circ$. Using this approach, the curvature angle φ_2 was found to change linearly with ray angle θ_1, as shown in Fig. 2(a). Using this curvature angle, the shape of the interface was calculated, and is presented in Fig. 2(b).

The resulting near field radiator is shown in Fig. 1(a). The device is fed with an RG402 coaxial cable ($r_{in} = 0.455$ mm, $r_{out} = 1.485$ mm), the center conductor of which has been extended by $p = 5.6$ mm, as shown in the inset of Fig. 1(a). The height of the overall structure is $h = 157.15$ mm.

The dielectric structure was fabricated using standard CNC machining (milling/lathing). The outer cladding was realized by applying a copper foil (3M$^{\text{TM}}$ 1126) to the dielectric structure and electrically connecting it to the outer conductor of the coaxial cable. A picture of the fabricated device is shown in Fig. 1(c).

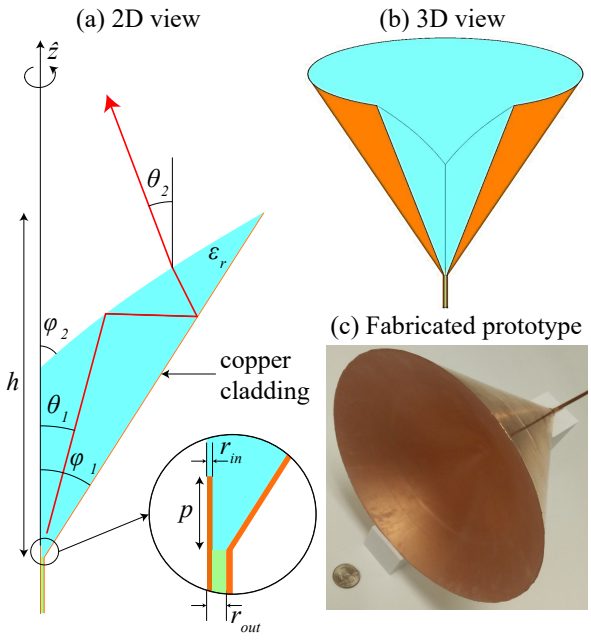

FIG. 1. (a) Cross-sectional view of the Bessel beam radiator with ray tracing diagram, (b) 3D view of device, and (c) picture of the fabricated prototype. A US quarter is also shown for comparison.

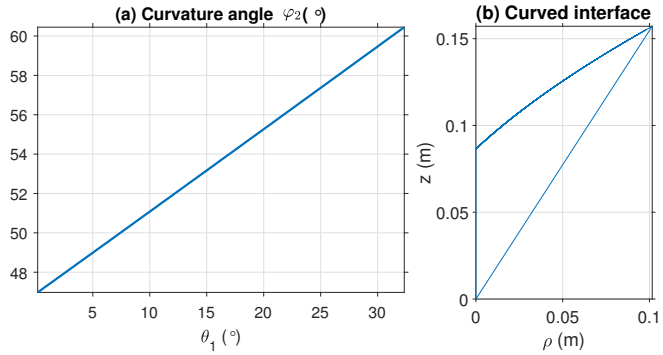

FIG. 2. (a) Curvature angle φ_2 as a function of ray angle θ_1 that maintains a constant cone angle $\theta_2 = 20^\circ$, and (b) the curved interface resulting from the changing φ_2 angle.

Next, the ability of the device to generate monochromatic TM Bessel beams is demonstrated. The radiated electric field has both longitudinal (z-directed) and radial (ρ-directed) components.

The longitudinal electric field of a non-apodized Bessel beam is a zeroth-order (φ-invariant) Bessel distribution

$$E_z(\rho, z) = J_0(k_0 \sin\theta_2 \rho) e^{j(\omega t - k_0 \cos\theta_2 z)}, \quad (2)$$

where k_0 is the free space wavenumber and θ_2 is the cone angle. A dependence of θ_2 on frequency results in beam dispersion. The geometrical optics design of the curved

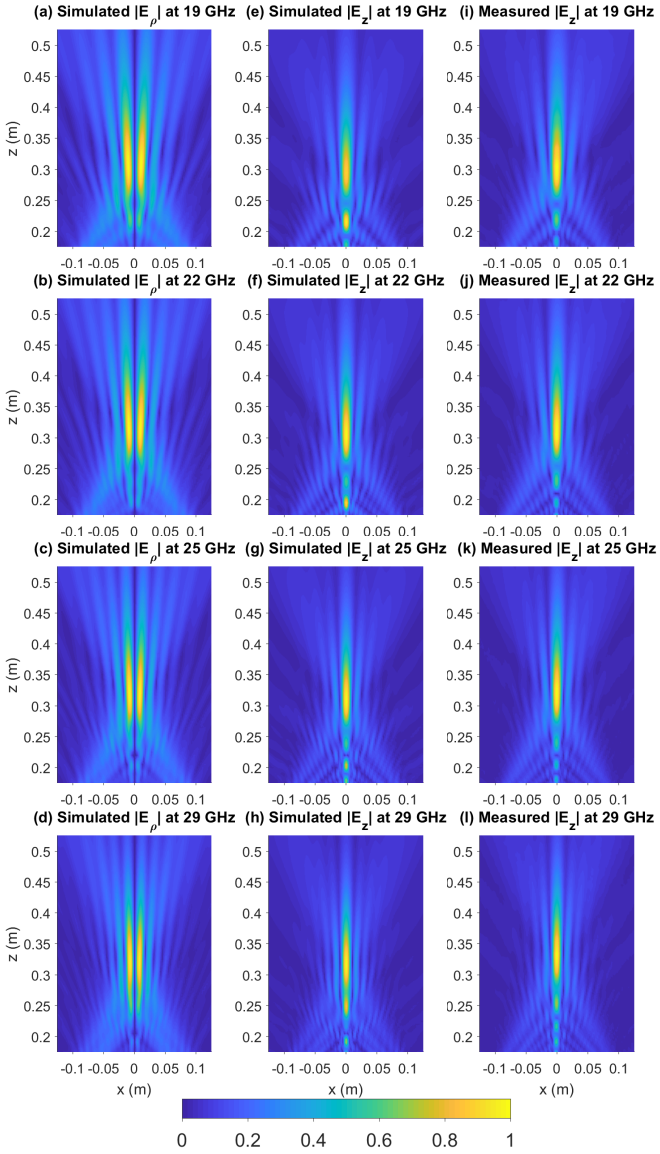

FIG. 3. Magnitude of the fields generated by the Bessel beam radiator at 19, 22, 25 and 29 GHz along the $y = 0$ plane: (a-d) simulated $|E_\rho|$, (e-h) simulated $|E_z|$, and (i-l) measured $|E_z|$.

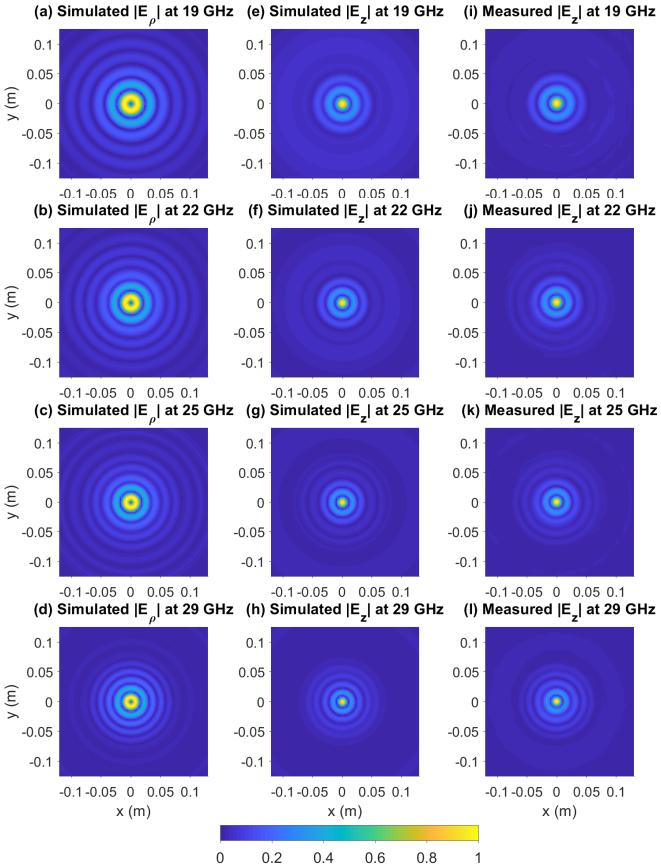

FIG. 4. Magnitude of the fields generated by the Bessel beam radiator at 19, 22, 25 and 29 GHz along the $z = 0.325$ m plane: (a-d) simulated $|E_\rho|$, (e-h) simulated $|E_z|$, and (i-l) measured $|E_z|$.

air-dielectric interface helps minimize dispersion (approximately 2° between 19 and 29 GHz), a phenomenon that results in degraded X Waves[24].

In Fig. 3, the magnitude of the fields generated by the radiator are presented at four frequencies: 19, 22, 25 and 29 GHz. Each row corresponds to one of these frequencies in increasing order from top to bottm. The simulated field components shown are the radial electric field (E_ρ) in the first column, and the longitudinal electric field (E_z) in the second column. COMSOL Multiphysics®, a commercially available finite element solver, was used to simulate the axially symmetric device. Finally, the measured E_z is plotted in the third column. The fields were measured using a coaxially-fed electric monopole acting as a probe, attached to a three-dimensional translation unit and a vector network analyzer.

The radial electric field exhibits the same spatial distribution as the azimuthal magnetic field (not shown for brevity) having a null along the z-axis, as expected from theory[14]. E_z possesses an apodized version of the profile given by Eq. 2, within the nondiffracting range of the device. The dielectric region preserves the polarization of the wave emitted by the coaxial cable. That is, the radial electric field in the coaxial cable excites a TM_z polarized Bessel beam. It is important to note that the radiated fields do not change significantly with frequency, meaning the device exhibits minimal dispersion.

In Fig. 4, the magnitude of the simulated E_ρ (first column) and simulated and measured E_z (second and third columns) along the $z = 0.325$ m plane are shown at the same four frequencies. In Fig. 5(a-d), the E_z quantities are plotted along the $y = 0$ line of the same plane, for a clearer comparison. Finally, Fig. 5(e-f) presents the angular distribution of the fields generated by the radiator, obtained by performing a spatial Fourier transform of E_z along the $z = 0.325$ m plane.

By squaring the angular distribution of E_ρ to obtain

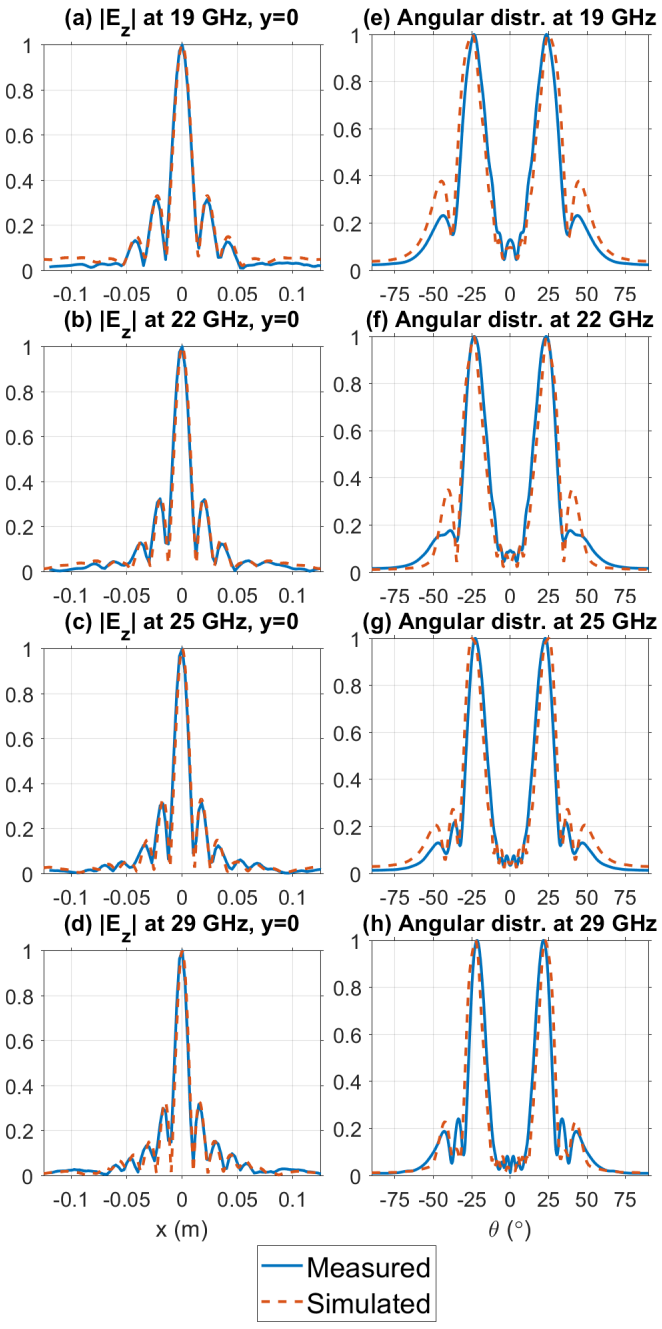

FIG. 5. Fields generated by the Bessel beam radiator at 19, 22, 25 and 29 GHz along the $z = 0.325$ m plane: (a-d) simulated and measured $|E_z|$ at $y = 0$, and (e-h) simulated and measured angular distribution of E_z.

power and integrating the power between the two local minima surrounding each peak, it is found that over 89% of the total radiated power is around the prescribed cone angle. Moreover, this angle does not change significantly with frequency meaning that all frequency components of a pulse emanated by the radiator possess approximately the same phase and group velocity: $v = c/\cos\theta_2$, where c is the speed of light. As a result, the pulse stays confined

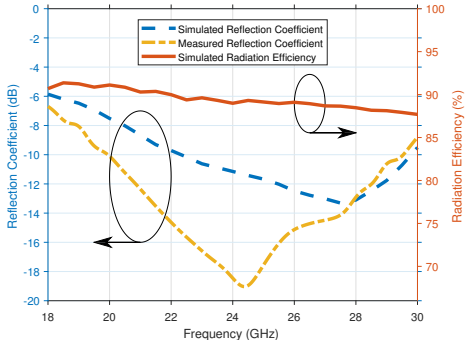

FIG. 6. Simulated (blue) and measured (yellow) reflection coefficient of the radiator (left axis), as well as radiation efficiency (red - right axis), as a function of frequency.

as it propagates.

In Fig. 6, the simulated and measured reflection coefficients of the structure are plotted as a function of frequency (left vertical axis). The conical flare acts as a wideband impedance matching mechanism, resulting in low reflections. The measured reflection coefficient is lower than the simulated one, due to the losses in the Rexolite region (the loss tangent is higher in this frequency range), and the slightly smoother transition from the coaxial cable to the Bessel beam radiator compared to simulation. The radiation efficiency of the structure is calculated in COMSOL as the ratio of power exiting the structure over the power that is input into it (right vertical axis). It can be seen that the radiator is highly efficient.

An X Wave is a pulse consisting of different frequency Bessel beams with the same cone angle. The wave function describing an X Wave (E_z for a TM$_z$ Bessel beam) is[24]:

$$\chi(\rho, z, t) = \int_{-\infty}^{\infty} F(k_0) J_0\left(k_0 \sin\theta_2 \rho\right) e^{jk_0(ct - \cos\theta_2 z)} dk_0, \tag{3}$$

where $F(k_0)$ are the spectral coefficients. For simplicity, assume that the frequency spectrum of the excitation signal applied to the input of the radiator is uniform from 22 to 29 GHz (widest bandwidth that can be obtained from the arbitrary waveform generator available to the authors). This leads to the input waveform pulse shown in Fig. 7(a).

Using the experimentally measured E_z along the $y = 0$ plane (captured at $N_f = 935$ frequency points between 22 and 29 GHz), the field generated under the pulse excitation of Fig. 7(a) is calculated. Specifically, for every point along the $y = 0$ plane, E_z can be calculated for any time t as

$$E_z(x, z, t) = \sum_{i=1}^{N_f} E_z(x, z, \omega_i) e^{j\omega_i t}, \tag{4}$$

where $E_z(x, z, \omega_i)$ denotes the measured field at each an-

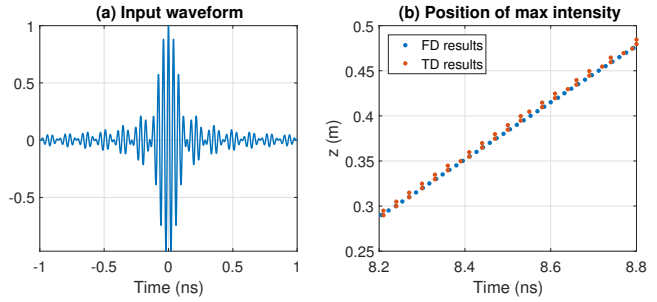

FIG. 7. (a) Uniform spectrum waveform (22-29 GHz) that is used to observe an X Wave, and (b) position of maximum intensity along the z-axis as a function of time for both frequency domain and time domain results.

gular frequency ω_i at (x, z)[24]. The intensity of E_z (normalized between 0 and 1) is plotted in Fig. 8(a-d) at four different times (t = 8.07, 8.30, 8.52, and 8.75 ns)[31]. The real part of E_z (normalized between -1 and 1) is plotted in Fig. 8(e-h). The generated fields are rotationally symmetric about the z-axis, meaning that a "bullet-like" pulse is emitted. The X wave is highly confined in the transverse plane and propagates with little dispersion and diffraction in the longitudinal direction within the nondiffracting range of the radiator: $z = 0.16$ to 0.44 m.

To further showcase the radiator's ability to produce X Waves, measurements were also performed in the time domain. The longitudinal electric field was again observed in the region above the radiator when excited with the waveform shown in Fig. 7(a). The details of the experimental procedure and the post-processing operations are given in[31]. The X Wave emitted by the radiator as a result of this sub-nanosecond input signal is presented at four time steps in Fig. 8(i-l).

The superluminal behavior of the X Wave[2] is verified in Fig. 7(b), which shows the position of maximum intensity along the z-axis as a function of time. From the linear regression of the frequency domain results, the velocity of the wave is found to be $v^{\mathrm{FD}} = c/\cos(17.85°) = 1.05c$, which is slightly lower than that from the linear regression of the time domain results: $v^{\mathrm{TD}} = c/\cos(19.29°) = 1.06c$. Both results are in line with the expected velocity from the COMSOL simulation: $c/\cos(18.70°) = 1.06c$.

To the best of the authors' knowledge, this is the first experimentally measured device capable of generating X Waves at microwave frequencies. Moreover, the vectorial nature of the fields has been thoroughly examined. The produced X waves exhibit polarization purity: a well-defined $\mathrm{TM_z}$ polarization.

The Bessel beam radiator, a device capable of generating TM polarized Bessel beams over a broad bandwidth, was reported. A geometrical optics design process was used to ensure that the Bessel beams emerge at a specified angle over a wide range of frequencies. First, the radiator's operation was verified in simulation. The device was then fabricated and tested, with measurements

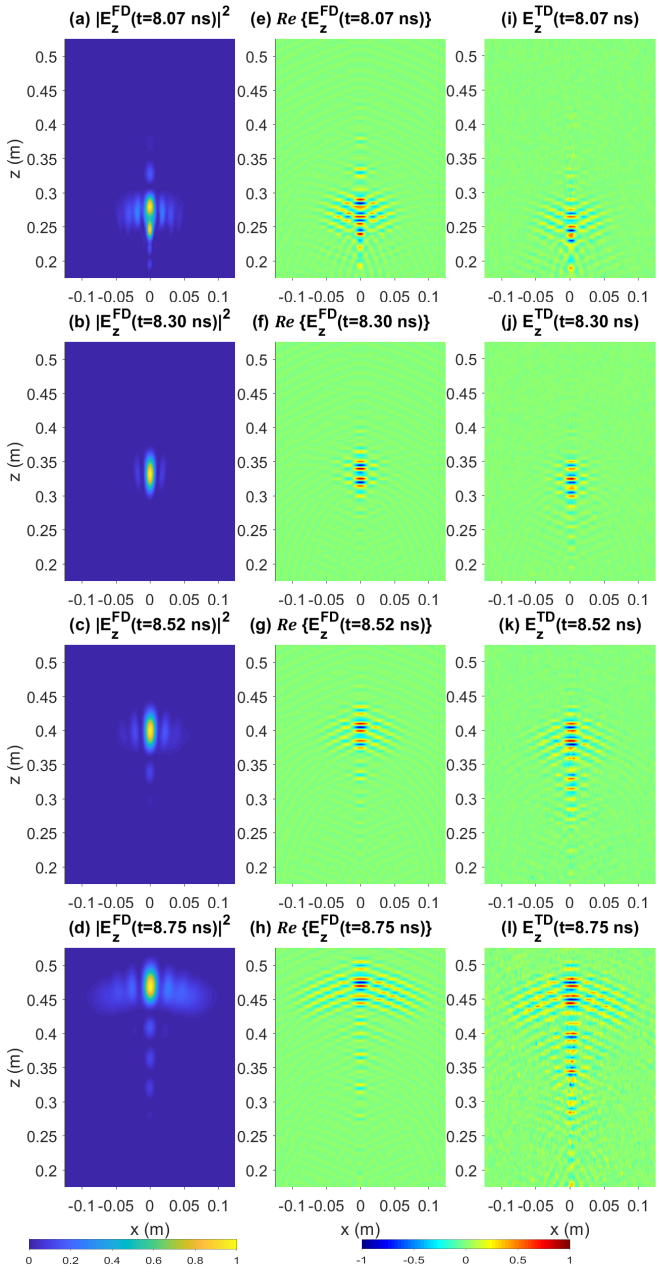

FIG. 8. (a-d) Instantaneous intensity of E_z in the region above the radiator based on frequency domain measurement results. The evolution of the X Wave can be seen at four different time steps. (e-h) Real part of E_z. (i-l) E_z in the region above the radiator based on time domain measurement results.

in close agreement with simulations. Through these measurements, it was shown that the radiator emits X Waves under a broadband excitation, the first such demonstration at microwave frequencies. This device can be used for high resolution near field imaging, wideband near field communication, or ground penetrating radar.

ACKNOWLEDGMENTS

This work was supported by the Air Force Office of Scientific Research (Grant No. FA9550-15-1-0101) and the National Science Foundation Materials Research Science and Engineering Center program DMR Grant No. 1120923. The prototype was fabricated at the LSA Scientific Instrument Shop at the University of Michigan.

* agrbic@umich.edu

[1] J. N. Brittingham, Journal of Applied Physics **54**, 1179 (1983).

[2] H. E. Hernández-Figueroa, M. Zamboni-Rached, and E. Recami, *Localized waves*, Vol. 194 (John Wiley & Sons, 2007).

[3] R. W. Ziolkowski, Physical Review A **39**, 2005 (1989).

[4] T. T. Wu, Journal of applied physics **57**, 2370 (1985).

[5] H. E. Moses and R. T. Prosser, SIAM Journal on Applied Mathematics **50**, 1325 (1990).

[6] J. Durnin, JOSA A **4**, 651 (1987).

[7] J.-y. Lu and J. F. Greenleaf, in *San Diego'92* (International Society for Optics and Photonics, 1992) pp. 92–119.

[8] C. Pfeiffer and A. Grbic, Physical Review B **91**, 115408 (2015).

[9] V. Grillo, J. Harris, G. C. Gazzadi, R. Balboni, E. Mafakheri, M. R. Dennis, S. Frabboni, R. W. Boyd, and E. Karimi, Ultramicroscopy **166**, 48 (2016).

[10] A. Marcinkevičius, S. Juodkazis, S. Matsuo, V. Mizeikis, and H. Misawa, Japanese Journal of Applied Physics **40**, L1197 (2001).

[11] R. Li, K. F. Ren, X. Han, Z. Wu, L. Guo, and S. Gong, Journal of Quantitative Spectroscopy and Radiative Transfer **126**, 69 (2013).

[12] J.-y. Lu and S. He, Optics Communications **161**, 187 (1999).

[13] S. Monk, J. Arlt, D. Robertson, J. Courtial, and M. Padgett, Optics Communications **170**, 213 (1999).

[14] M. Ettorre and A. Grbic, IEEE Transactions on Antennas and Propagation **60**, 3605 (2012).

[15] C. Pfeiffer and A. Grbic, Physical Review Applied **2**, 044012 (2014).

[16] M. Q. Qi, W. X. Tang, and T. J. Cui, Scientific reports **5** (2015).

[17] G. Scott and N. McArdle, Optical Engineering **31**, 2640 (1992).

[18] F. Aieta, P. Genevet, M. A. Kats, N. Yu, R. Blanchard, Z. Gaburro, and F. Capasso, Nano letters **12**, 4932 (2012).

[19] W. Williams and J. Pendry, JOSA A **22**, 992 (2005).

[20] J. Turunen, A. Vasara, and A. T. Friberg, Applied optics **27**, 3959 (1988).

[21] J.-Y. Lu and J. F. Greenleaf, IEEE Transactions on Ultrasonics, Ferroelectrics, and Frequency Control **39**, 19 (1992).

[22] P. Saari and K. Reivelt, Physical Review Letters **79**, 4135 (1997).

[23] P. Bowlan, H. Valtna-Lukner, M. Lõhmus, P. Piksarv, P. Saari, and R. Trebino, Optics letters **34**, 2276 (2009).

[24] W. Fuscaldo, S. C. Pavone, G. Valerio, A. Galli, M. Albani, and M. Ettorre, Journal of Applied Physics **119**, 194903 (2016).

[25] D. Mugnai, A. Ranfagni, and R. Ruggeri, Physical review letters **84**, 4830 (2000).

[26] B. Allen, M. Dohler, E. Okon, W. Malik, A. Brown, and D. Edwards, *Ultra wideband antennas and propagation for communications, radar and imaging* (John Wiley & Sons, 2006).

[27] K. Stephan, J. Mead, D. Pozar, L. Wang, and J. Pearce, IEEE Transactions on Antennas and Propagation **55**, 1199 (2007).

[28] V. Chawla and D. S. Ha, IEEE Communications Magazine **45**, 11 (2007).

[29] S. Karimkashi and A. A. Kishk, IEEE Transactions on Antennas and Propagation **57**, 3813 (2009).

[30] N. Chiotellis and A. Grbic, in *Antennas and Propagation (APSURSI), 2016 IEEE International Symposium on* (IEEE, 2016) pp. 873–874.

[31] See Supplemental Material at [URL] for a detailed treatment of the effects of finite bandwidth, frequency dispersion and aperture apodization on the shape of the emitted pulse and additional details regarding the time domain measurements.